

# Whistler anisotropy instability at low electron $\beta$ : Particle-in-cell simulations

S. Peter Gary,<sup>\*</sup> Kaijun Liu,<sup>†</sup> and Dan Winske<sup>‡</sup>

*Los Alamos National Laboratory, Los Alamos, NM 87545*

(Dated: April 21, 2011)

## Abstract

The whistler anisotropy instability is studied in a magnetized, homogeneous, collisionless plasma model. The electrons (denoted by subscript  $e$ ) are represented initially with a single bi-Maxwellian velocity distribution with a temperature anisotropy  $T_{\perp e}/T_{\parallel e} > 1$  where  $\perp$  and  $\parallel$  denote directions perpendicular and parallel to the background magnetic field  $\mathbf{B}_o$ , respectively. Kinetic linear dispersion theory predicts that, if the ratio of the electron plasma frequency  $\omega_e$  to the electron cyclotron frequency  $\Omega_e$  is greater than unity and  $\beta_{\parallel e} \geq 0.025$ , the maximum growth rate of this instability is at parallel propagation, where the fluctuating fields are strictly electromagnetic. At smaller values of  $\beta_{\parallel e}$ , however, the maximum growth rate shifts to propagation oblique to  $\mathbf{B}_o$  and the fluctuating electric fields become predominantly electrostatic. Linear theory and two-dimensional particle-in-cell simulations are used to examine the consequences of this transition. Three simulations are carried out, with initial  $\beta_{\parallel e} = 0.10, 0.03$ , and  $0.01$ . The fluctuating fields of the  $\beta_{\parallel e} = 0.10$  run are predominantly electromagnetic, with nonlinear consequences similar to those of simulations already described in the literature. In contrast, the growth of fluctuations at oblique propagation in the low electron  $\beta$  runs leads to a significant  $\delta E_{\parallel}$  which heats the electrons leading to the formation of a substantial suprathermal component in the electron parallel velocity distribution.

## I. INTRODUCTION

A mode frequently observed in the terrestrial magnetosphere is the whistler, which propagates in a frequency range  $\Omega_{lh} \lesssim \omega_r < |\Omega_e|$  where the lower hybrid frequency  $\Omega_{lh} \simeq \sqrt{\Omega_p |\Omega_e|}$  and  $\Omega_j$  represents the cyclotron frequency of the  $j$ th species of a plasma. Whistlers can be excited by several different sources in the magnetosphere where they, in turn, react back upon the plasmas via both quasilinear and nonlinear processes. Here we describe a study of the whistler anisotropy instability driven by the electron temperature anisotropy  $T_{\perp e}/T_{\parallel e} > 1$ , where  $\perp$  and  $\parallel$  denote directions perpendicular and parallel to the background magnetic field  $\mathbf{B}_o$ , respectively. We have used both kinetic linear dispersion theory and two-dimensional particle-in-cell (PIC) simulations to examine the fundamental properties of this growing mode and its consequences for the electron velocity distribution as functions of  $\beta_{\parallel e}$ .

Linear dispersion theory predicts that, at sufficiently large  $\beta_{\parallel e}$  and  $\omega_e/|\Omega_e| > 1$  (Here  $\omega_e$  denotes the electron plasma frequency), a sufficiently large electron temperature anisotropy  $T_{\perp e}/T_{\parallel e} > 1$  drives this instability with  $kc/\omega_e < 1$  and maximum growth rate at  $\mathbf{k} \times \mathbf{B}_o = 0$  (e.g., [1], Chapter 7). This is the electromagnetic regime of this instability, because  $\delta E_{\parallel} \simeq 0$  and  $\delta B_{\parallel} \simeq 0$  so that both  $\delta B$  and  $\delta E$  are transverse to  $\mathbf{B}_o$ . As  $\beta_{\parallel e}$  decreases, a successively larger electron anisotropy is needed to excite the instability ([2]) until near  $\beta_{\parallel e} \simeq 0.025$ , the maximum growth rate shifts from parallel to oblique propagation relative to  $\mathbf{B}_o$  ([3], [4], [5], [6], [7]). In this regime, the fluctuating electric fields become predominantly electrostatic with  $\mathbf{k} \cdot \delta \mathbf{E} \simeq k\delta E$ . Nevertheless, the fluctuating magnetic fields remain non-zero, so [4] termed this the quasi-electrostatic regime of this instability. We have used kinetic linear dispersion theory to examine the details of this transition.

Linear dispersion theory not only provides a relationship between the complex frequency and wavevector  $\mathbf{k}$  for a particular normal mode, it also yields dimensionless ratios of quadratic combinations of the various fluctuating field components of that mode [e.g., Chapter 5 of [1]]. For example, linear theory yields the fluctuating magnetic field ratios  $|\delta B_j|^2/|\delta \mathbf{B}|^2$  and the fluctuating electric field ratios  $|\delta E_j|^2/|\delta \mathbf{E}|^2$  as functions of the frequency and wavevector. We define the electrostatic ratio of the fluctuating electric fields to be

$$R_{es} \equiv \frac{|\hat{\mathbf{k}} \cdot \delta \mathbf{E}|^2}{|\delta \mathbf{E}|^2}$$

and the electric/magnetic field energy ratio as

$$\sigma_{EE} \equiv \frac{|\delta \mathbf{E}|^2}{|\delta \mathbf{B}|^2} \quad (1)$$

([1], Eq. (5.2.5)).

We have further used two-dimensional PIC simulations to study the nonlinear properties of this instability during the transition from the strictly electromagnetic regime to the predominantly electrostatic domain. A number of PIC simulations have been carried out in homogeneous plasma models for the former case, both one-dimensional ([8], [9], [10], [11], [12]) and two-dimensional ([10], [2]; [13]), but there have been relatively few such computations in the latter low- $\beta$  case ([13]; [7]). The primary wave-particle interaction for electromagnetic fluctuations at  $\mathbf{k} \times \mathbf{B}_o = 0$  is the cyclotron resonance, and its primary consequence is pitch-angle scattering. At sufficiently oblique propagation, however, the Landau resonance plays an increasing role in particle scattering, and particle heating parallel to  $\mathbf{B}_o$  should become important. Thus, as we simulate this instability at successively smaller values of  $\beta_{\parallel e}$ , our results show evidence of the transition from electron pitch-angle scattering to parallel heating.

We denote the  $j$ th species plasma frequency as  $\omega_j \equiv \sqrt{4\pi n_o e^2 / m_j}$ , the  $j$ th species cyclotron frequency as  $\Omega_j \equiv e_j B_o / m_j c$ , the  $j$ th component inertial length  $\lambda_j \equiv c / \omega_j$ , the  $j$ th component thermal speed as  $v_j \equiv \sqrt{k_B T_{\parallel j} / m_j}$ , and  $\beta_{\parallel j} \equiv 8\pi n_j k_B T_{\parallel j} / B_o^2$ . The Alfvén speed is  $v_A \equiv B_o / \sqrt{4\pi n_o m_i}$ . Here  $n_o$  is the total plasma density,  $\mathbf{B}_o$  denotes the uniform background magnetic field, and we consider a two-species plasma of electrons (subscript  $e$ ) and protons (subscript  $p$ ).

The Cartesian coordinate system of our linear dispersion theory ([1]) admits spatial variations in both the direction parallel to  $\mathbf{B}_o$  (denoted by  $\parallel$ ) and one direction perpendicular to the background field (denoted by  $\perp$ ), but no spatial variations in the other perpendicular direction (denoted by  $\perp\perp$ ). So for our linear theory the real wavevector is  $\mathbf{k} = \hat{\mathbf{z}}k_{\parallel} + \hat{\mathbf{y}}k_{\perp} = \hat{\mathbf{z}}k \cos\theta + \hat{\mathbf{y}}k \sin\theta$  where  $\theta$  denotes the wavevector direction relative to  $\mathbf{B}_o$ . The complex frequency is  $\omega = \omega_r + i\gamma$  where  $\gamma > 0$  represents temporal growth of a normal mode of the plasma. For a given set of plasma parameters,  $\gamma_m$  denotes the maximum growth rate taken over all magnitudes and directions of  $\mathbf{k}$ , and  $\omega_m$ ,  $k_m$  and  $\theta_m$  denote the corresponding real frequency, wavenumber and angle of propagation, respectively.

## II. LINEAR THEORY

This section describes results from numerical solutions of the full electromagnetic linear kinetic dispersion equation for bi-Maxwellian velocity distributions ([1]) without approximation. The proton velocity distribution in each case is an isotropic Maxwellian, and the electron velocity distribution is a single bi-Maxwellian with  $T_{\perp e}/T_{\parallel e} > 1$ . The following values are assumed:  $m_p/m_e = 1836$ ,  $\omega_e/|\Omega_e| = 4.0$ ,  $T_{\parallel e}/T_p = 1.0$ , and  $T_{\perp p} = T_{\perp e} = T_p$ .

Figure 1 compares  $\gamma(\mathbf{k})$  near a maximum growth rate of  $\gamma_m/|\Omega_e| = 0.01$  as a function of the propagation angle for two cases:  $\beta_{\parallel e} = 0.10$  and  $T_{\perp e}/T_{\parallel e} = 2.25$ , when  $\gamma_m$  is at parallel propagation, and  $\beta_{\parallel e} = 0.01$  and  $T_{\perp e}/T_{\parallel e} = 3.78$ , when maximum growth is at oblique propagation. At  $0.10 \leq \beta_{\parallel e} \leq 10$ , the maximum growth rate remains at parallel propagation and, although it is not shown here, the cone of unstable modes at  $k_m v_e/|\Omega_e|$  remains confined to  $\theta < 30^\circ$ .

Figure 2 compares the fluctuating field ratios near maximum growth in the two cases illustrated in Figure 1. At  $\beta_{\parallel e} = 0.10$  the fluctuations are predominantly electromagnetic, but at  $\beta_{\parallel e} = 0.01$ , the compressive magnetic component  $\delta B_{\parallel}$  becomes appreciable and the electrostatic component dominates the fluctuating electric field, i.e.  $0.98 < R_{es} < 1.0$  (not shown).

Figure 3 illustrates some properties of the whistler anisotropy instability at  $\gamma_m/|\Omega_e| = 0.01$  as functions of  $\beta_{\parallel e}$ . In the electromagnetic regime, the maximum growth rate is at propagation parallel to  $\mathbf{B}_o$ , both  $k_m c/\omega_e$  and  $k_m v_e/|\Omega_e|$  provide weak variations as  $\beta_{\parallel e}$  varies by more than two orders of magnitude, the anisotropy at instability threshold,  $T_{\perp e}/T_{\parallel e} - 1$ , scales roughly as the inverse of  $\sqrt{\beta_{\parallel e}}$  as in [5], and  $\sigma_{EE} \ll 1$ . But in the predominantly electrostatic regime at  $\beta_{\parallel e} < 0.025$ , the maximum growth rate changes to distinctly oblique propagation. Furthermore,  $\omega_r/|\Omega_e|$ ,  $\theta_m$ ,  $k_m v_e/|\Omega_e|$ , and the electron temperature anisotropy all approach constant asymptotic values as  $\beta_{\parallel e}$  diminishes toward zero.

Further, we have used our kinetic linear dispersion code to examine parametric variations of the critical value of  $\beta_{\parallel e}$ , that is, the value at which the maximum growth rate undergoes a transition from parallel propagation to oblique propagation. We find that this critical  $\beta_{\parallel e}$  is essentially independent of  $\omega_e/|\Omega_e|$  as long as  $\omega_e/|\Omega_e| > 1$ , and that it is a rather weak function of the instability growth rate, satisfying  $0.022 \lesssim \beta_{\parallel e} \lesssim 0.025$  over two orders of magnitude variation in the maximum growth rate, i.e.,  $0.001 \leq \gamma_m/|\Omega_e| \leq 0.10$ .

### III. PARTICLE-IN-CELL SIMULATIONS

This section describes particle-in-cell simulations of the whistler anisotropy instability carried out in a magnetized, homogeneous, collisionless plasma model. Our concern here is whistler fluctuations at  $\omega_r \gg \Omega_p$ , so the protons are treated as an immobile, charge neutralizing background to conserve computation time, as in [2] and [7]. The initial electron velocity distribution is a single bi-Maxwellian with  $T_{\perp e}/T_{\parallel e} > 1$ . Initial conditions on the dimensionless plasma parameters are  $m_p/m_e = 1836$  and  $\omega_e/|\Omega_e| = 4.0$ . The two-dimensional simulation domain lies in the  $x$ - $y$  plane with  $\mathbf{B}_o$  in the  $x$ -direction, so  $\mathbf{k} \equiv \hat{\mathbf{x}}k_{\parallel} + \hat{\mathbf{y}}k_{\perp}$ . Periodic boundary conditions are used in both spatial directions, the number of cells in the simulations are  $N_{\parallel} \times N_{\perp} = 64 \times 64 = 4096$ , and the simulation time step is  $\Omega_p \Delta t = 0.00001$ . There are 9600 simulation particles in each cell at  $t = 0$ .

Kinetic linear dispersion theory (see Section 2) shows that, for the case of a single bi-Maxwellian electron distribution considered as the initial condition here, the whistler anisotropy instability typically has maximum growth rate at  $\mathbf{k} \times \mathbf{B}_o = 0$  if  $\beta_{\parallel e} \geq 0.025$ , whereas the maximum growth rate shifts to oblique propagation at  $40^\circ \lesssim \theta \lesssim 50^\circ$  for  $\beta_{\parallel e} < 0.025$ . To study the nonlinear consequences of this fundamental change in propagation, we have carried out three PIC simulations, all with initial parameters corresponding to linear theory maximum growth rates of  $\gamma_m/|\Omega_e| = 0.03$ . Run 1 begins with  $\beta_{\parallel e} = 0.10$  and  $T_{\perp e}/T_{\parallel e} = 2.75$ ; linear theory predicts that the maximum growth rate is at  $k_m \lambda_e = 1.0$  and  $\theta_m = 0^\circ$ . For this run we chose a simulation box size of  $L_{\parallel} = L_{\perp} = 1.2\lambda_p$ . For Run 2, the initial plasma parameters are  $\beta_{\parallel e} = 0.03$  and  $T_{\perp e}/T_{\parallel e} = 4.1$ ; the corresponding maximum growth rate is at  $k_m \lambda_e = 1.3$  and  $\theta_m = 0^\circ$ . For this run our simulation box size is  $L_{\parallel} = L_{\perp} = 0.6\lambda_p$ . For Run 3, the initial plasma parameters are  $\beta_{\parallel e} = 0.01$  and  $T_{\perp e}/T_{\parallel e} = 5.0$ ; the corresponding maximum growth rate is at  $k_m \lambda_e = 3.8$  and  $\theta_m = 48^\circ$ . Here we used a box size of  $L_{\parallel} = L_{\perp} = 0.3\lambda_p$ . For  $\omega_e/|\Omega_e| = 4.0$ , Eq. (4) of [13] implies an electron parallel temperature of 1.6 keV for Run 1 at  $\beta_{\parallel e} = 0.10$ , and  $k_B T_{\parallel e} = 160$  eV for Run 3 with  $\beta_{\parallel e} = 0.01$ .

Figure 4 presents linear theory growth rates as functions of  $k$  and  $\theta$  for the initial parameters of the three runs as stated above. The  $\beta_{\parallel e} = 0.10$  case of Run 1 has maximum growth rate at  $\mathbf{k} \times \mathbf{B}_o = 0$ , with weaker growth at oblique propagation. The  $\beta_{\parallel e} = 0.03$  case of Run 2 also has maximum growth rate at  $\mathbf{k} \times \mathbf{B}_o = 0$ , but weaker growth extends to more oblique

propagation. For the  $\beta_{\parallel e} = 0.01$  case of Run 3, the maximum growth rate has shifted to oblique propagation, although weaker growth persists at  $\mathbf{k} \times \mathbf{B}_o = 0$ .

This prediction is confirmed by the simulation results illustrated in Figure 5 which compares the two-dimensional spectra of  $\delta B_{\perp\perp}$  during the linear growth phase of all three runs as functions of both wavevector and position. The enhanced fluctuations of Run 1 display essentially vertical wavefronts which correspond to  $\mathbf{k} \times \mathbf{B}_o \simeq 0$ , whereas the wavefronts from Run 2 indicate some departures from strictly vertical, consistent with the increasing importance of fluctuation growth at oblique propagation. Finally, the wavefronts of Run 3 are at distinctly oblique directions of propagation consistent with the linear theory prediction of  $\theta = 48^\circ$  at maximum growth rate.

Figure 6 compares the electron temperature anisotropy, the fluctuating magnetic field component energies, and the fluctuating electric field component energies as functions of time for the three runs. In all three cases, the early-time ( $0 \leq |\Omega_e|t \leq 300$ ) response of the instability is exponential growth at rates somewhat less than that predicted by linear theory; here  $\gamma/|\Omega_e| \simeq 0.01$  for Run 1 and  $\gamma/|\Omega_e| \simeq 0.02$  for Run 3. In agreement with the linear theory predictions of Figure 2, the fluctuating field energy densities for electromagnetic Run 1 satisfy  $|\delta B_{\parallel}|^2 \ll |\delta B_{\perp}|^2 \lesssim |\delta B_{\perp\perp}|^2$  and  $|\delta E_{\parallel}|^2 \ll |\delta E_{\perp\perp}|^2 \lesssim |\delta E_{\perp}|^2$  whereas for the predominantly electrostatic Run 3  $|\delta B_{\parallel}|^2 \simeq |\delta B_{\perp}|^2 < |\delta B_{\perp\perp}|^2$  and  $|\delta E_{\perp\perp}|^2 \ll |\delta E_{\parallel}|^2 < |\delta E_{\perp}|^2$ . Furthermore, as one might expect, the maximum value of  $|\delta \mathbf{B}|^2/B_o^2$  decreases by an order of magnitude with a factor of ten decrease in  $\beta_{\parallel e}$ . In contrast, the saturation value of  $|\delta \mathbf{E}|^2/B_o^2$  shows a modest increase as  $\beta_{\parallel e}$  decreases.

After saturation, Figure 6 further shows the usual temporal decrease of the electron temperature anisotropy and the fluctuating field energies ([2], [10]; [12]). However, there are quantitative differences in the late time responses. Specifically, the overall percentages of late-time decreases in  $T_{\perp e}/T_{\parallel}$ ,  $|\delta \mathbf{B}|^2/B_o$ , and  $|\delta \mathbf{E}|^2/B_o$  increase from the  $\beta_{\parallel e} = 0.10$  Run 1 to the  $\beta_{\parallel e} = 0.01$  Run 3. This is apparently due to the increasing excitation of oblique modes which are subject to Landau damping so that the transfer of energy from electrons to waves during instability growth is reversed and wave dissipation and electron heating takes place.

Figure 7 illustrates the reduced electron velocity distribution  $f_e(v_{\parallel})$  at  $|\Omega_e|t = 0$  and 1836 for all three runs. For Run 1  $|\delta \mathbf{E}|^2 \ll |\delta \mathbf{B}|^2$  and pitch-angle scattering by the magnetic fluctuations is the primary electron transport process. The late-time velocity distribution

from Run 1 shows weak transport of electrons from thermal to suprathermal speeds, but no significant departure from the overall Maxwellian shape. In contrast, the late-time  $f_e(v_{\parallel})$  from Run 3 shows much stronger electron heating, with substantial energy gain which appears as a new suprathermal component (Fig. 5 of [13]; Fig. 14 of [7]). Our interpretation of this suprathermal electron heating is that it is the result of two separate wave-particle interactions acting in tandem. First, there is pitch-angle scattering via the electron cyclotron resonance with the  $\delta B_{\perp\perp}$  and  $\delta B_{\perp}$  (which remain relatively large even at oblique propagation); as in the electromagnetic Run 1, this transports electrons from larger to smaller pitch angles without substantial change in particle energy. Second, there is heating parallel to  $\mathbf{B}_o$  via the electron Landau resonance with  $\delta E_{\parallel}$  (which is zero for the dominant parallel-propagating fluctuations of the electromagnetic case but significant at oblique propagation, as indicated by Figure 2b) which substantially increases the kinetic energy of the suprathermal electrons.

Figure 8 provides further insight into this suprathermal electron heating by illustrating a detail from  $f_e(v_{\parallel})$  at four different times during Run 3. The image shows a gradual increase in the number of electrons in the range  $3 \lesssim |v_{\parallel}|/v_e \lesssim 6$  as simulation time progresses, but no important increase in the electron flux at  $6 < |v_{\parallel}|/v_e$ . This is consistent with the scenario that this heating is due to the Landau resonant interaction between  $\delta E_{\parallel}$  and the parallel component of electron velocities. At maximum growth linear theory for the initial conditions of Run 3 predicts  $\omega_r/k_{\parallel}v_e \simeq 3.9$ , so the parallel electric fields are strongly scattering electrons near  $v_{\parallel} \simeq 3.9v_e$ , allowing the particles to move down the gradient of the velocity distribution to become the suprathermal component illustrated in Figures 7 and 8. This component is not well fit by either a hot Maxwellian or a kappa-type parallel velocity distribution.

#### IV. CONCLUSIONS

We have carried out particle-in-cell simulations of the whistler anisotropy instability driven by a temperature anisotropy  $T_{\perp e}/T_{\parallel e} > 1$  on an initially bi-Maxwellian electron velocity distribution. Linear theory predicts that, at  $\beta_{\parallel e} \geq 0.025$ , the maximum growth rate of this instability is at propagation parallel to  $\mathbf{B}_o$  and the fluctuating fields are primarily electromagnetic. At smaller values of  $\beta_{\parallel e}$ , the maximum growth rate shifts to oblique propagation and the electric field fluctuations become predominantly electrostatic. The sim-

ulations confirm these predictions of linear theory. Furthermore, the  $\beta_{\parallel e} = 0.01$  and 0.03 simulations show that the  $\delta E_{\parallel}$  from the growth of fluctuations at oblique propagation leads to the formation of a substantial suprathermal component in the electron parallel velocity distribution.

## ACKNOWLEDGMENTS

This work was performed under the auspices of the U.S. Department of Energy (DOE). It was supported in part by the Defense Threat Reduction Agency under the “Basic Research for Combating Weapons of Mass Destruction (WMD)” Program, projects IACRO 10-4946I and IACRO 10-4284I, and in part by the Dynamic Radiation Environment Assimilation Model (DREAM) Project at Los Alamos National Laboratory.

---

\* pgary@lanl.gov

† kaijun@lanl.gov

‡ winske@lanl.gov

- [1] S. P. Gary, *Theory of Space Plasma Microinstabilities* (Cambridge University Press, New York, 1993).
- [2] S. P. Gary and J. Wang, J. Geophys. Res., **101**, 10,749 (1996).
- [3] K. Hashimoto and I. Kimura, J. Geophys. Res., **86**, 11,148 (1981).
- [4] N. Ohmi and M. Hayakawa, J. Plasma Phys., **35**, 351 (1986).
- [5] S. P. Gary and I. H. Cairns, J. Geophys. Res., **104**, 19,835 (1999).
- [6] O. Santolik, D. A. Gurnett, J. S. Pickett, S. Grimald, P. M. E. Décreau, M. Parrot, N. Cornilleau-Wehrin, F. El-Lemdani Mazouz, D. Schriver, N. P. Meredith, and A. Fazakerley, J. Geophys. Res., **115**, A00F16, (2010).
- [7] D. Schriver, M. Ashour-Abdalla, F. V. Coroniti, J. N. LeBoeuf, V. Decyk, P. Travnicek, O. Santolik, D. Winningham, J. S. Pickett, M. L. Goldstein, and A. N. Fazakerley, J. Geophys. Res., **115**, A00F17 (2010).
- [8] S. L. Ossakow, I. Haber, and E. Ott, Phys. Fluids, **15**, 1538 (1972).
- [9] S. Cuperman, Revs. Geophys. Space Physics, **19**, 307 (1981).



- [10] P. E. Devine, S. C. Chapman, and J. W. Eastwood, *J. Geophys. Res.*, **100**, 17,189 (1995).
- [11] Q. Lu, L. Wang, Y. Zhou, and S. Wang, *Chin. Phys. Lett.*, **21**, 129 (2004).
- [12] Q. Lu, L. Zhou, and S. Wang, *J. Geophys. Res.*, **115**, A02213 (2010).
- [13] S. P. Gary, D. Winske, and M. Hesse, *J. Geophys. Res.*, **105**, 10,751 (2000).

FIG. 1: The linear growth rate of the whistler anisotropy instability as a function of the angle of propagation for three different values of  $kv_p/\Omega_p$  as labeled. Here and in Figures 2, 3, and 4,  $m_p/m_e = 1836$ ,  $\omega_e/|\Omega_e| = 4.0$ ,  $T_{\parallel e}/T_p = 1.0$ , and  $T_{\perp p} = T_{\perp e} = T_p$ . Further,  $\beta_{\parallel e}$  and the electron anisotropies are chosen to yield  $\gamma_m/|\Omega_e| = 0.01$ . (a)  $\beta_{\parallel e} = 0.10$  and  $T_{\perp e}/T_{\parallel e} = 2.25$ . (b)  $\beta_{\parallel e} = 0.01$  and  $T_{\perp e}/T_{\parallel e} = 3.78$ .

FIG. 2: Linear theory results: The fluctuating field ratios for the whistler anisotropy instability as functions of the angle of propagation for the wavenumbers of maximum growth rate using the same parameters as stated in the caption of Figure 1. (a) Fluctuating magnetic field ratios and (b) fluctuating electric field ratios.

FIG. 3: Linear properties of the whistler anisotropy instability at  $\gamma_m/|\Omega_e| = 0.01$  as functions of  $\beta_{\parallel e}$ . (a) The real frequency, (b) the angle of propagation, (c) the magnitude of the wavenumber, (d) the electron temperature anisotropy, and (e) the electric/magnetic field energy ratio [Equation (1)]. For all cases at which the maximum growth rate is at oblique propagation, that is,  $0.001 < \beta_{\parallel e} < 0.025$ ,  $\omega_r/k_{\parallel}v_e \simeq 4.05$ .

FIG. 4: The linear growth rate of the whistler anisotropy instability as a function of wavenumber  $k$  and angle of propagation  $\theta$  for the initial plasma parameters of the three simulations defined in the text: (a) Run 1 with  $\beta_{\parallel e} = 0.10$ , (b) Run 2 with  $\beta_{\parallel e} = 0.03$ , and (c) Run 3 with  $\beta_{\parallel e} = 0.01$ . The heavy black lines in each panel correspond to the condition  $\gamma/|\Omega_e| = 0.02$ . The asterisk in each panel represents the maximum growth rate of  $\gamma_m/|\Omega_e| = 0.03$ . Note that the minimum value of the color scale corresponds to  $\gamma_m/|\Omega_e| = -0.03$  so that larger damping rates saturate in the plot.

FIG. 5: PIC simulation results at  $|\Omega_e|t = 184$  for (left column)  $\delta B_{\perp\perp}(x, y)$  and (right column)  $\delta B_{\perp\perp}(k_{\parallel}, k_{\perp})$ . The heavy black lines of the right-hand panels correspond to the black lines of Figure 4, that is, the condition  $\gamma/|\Omega_e| = 0.02$ .

FIG. 6: PIC simulation results: The electron temperature anisotropy, the fluctuating magnetic field component energies, and the fluctuating electric field component energies as functions of time for (a) (d) (g) Run 1 with  $\beta_{\parallel e} = 0.10$ , (b) (e) (h) Run 2 with  $\beta_{\parallel e} = 0.03$ , and (c) (f) (i) Run 3 with  $\beta_{\parallel e} = 0.01$ . In panels (d) (e) and (f), the red lines denote  $|\delta B_{\parallel}|^2/B_o^2$ , the green lines denote  $|\delta B_{\perp}|^2/B_o^2$ , the blue lines denote  $|\delta B_{\perp\perp}|^2/B_o^2$ , and the black lines denote  $|\delta \mathbf{B}|^2/B_o^2$ . In panels (g) (h) and (i), the red lines denote  $|\delta E_{\parallel}|^2/B_o^2$ , the green lines denote  $|\delta E_{\perp}|^2/B_o^2$ , the blue lines denote  $|\delta E_{\perp\perp}|^2/B_o^2$ , and the black lines denote  $|\delta \mathbf{E}|^2/B_o^2$ .

FIG. 7: PIC simulation results for the reduced electron velocity distribution  $f_e(v_{\parallel})$  (a) Run 1 with  $\beta_{\parallel e} = 0.10$ , (b) Run 2 with  $\beta_{\parallel e} = 0.03$ , and (c) Run 3 with  $\beta_{\parallel e} = 0.01$ . The dashed curves represent the initial Maxwellian distributions, and the solid curves display the parallel velocity distributions at  $|\Omega_e|t = 1836$ .

FIG. 8: PIC simulation results from Run 3 for part of the reduced electron velocity distribution  $f_e(v_{\parallel})$  at four simulation times. The dashed line represents the initial Maxwellian distribution, the dotted line corresponds to  $|\Omega_e|t = 367$ , the long-dash-short-dashed line corresponds to  $|\Omega_e|t = 918$ , and the solid line corresponds to  $|\Omega_e|t = 1836$ .

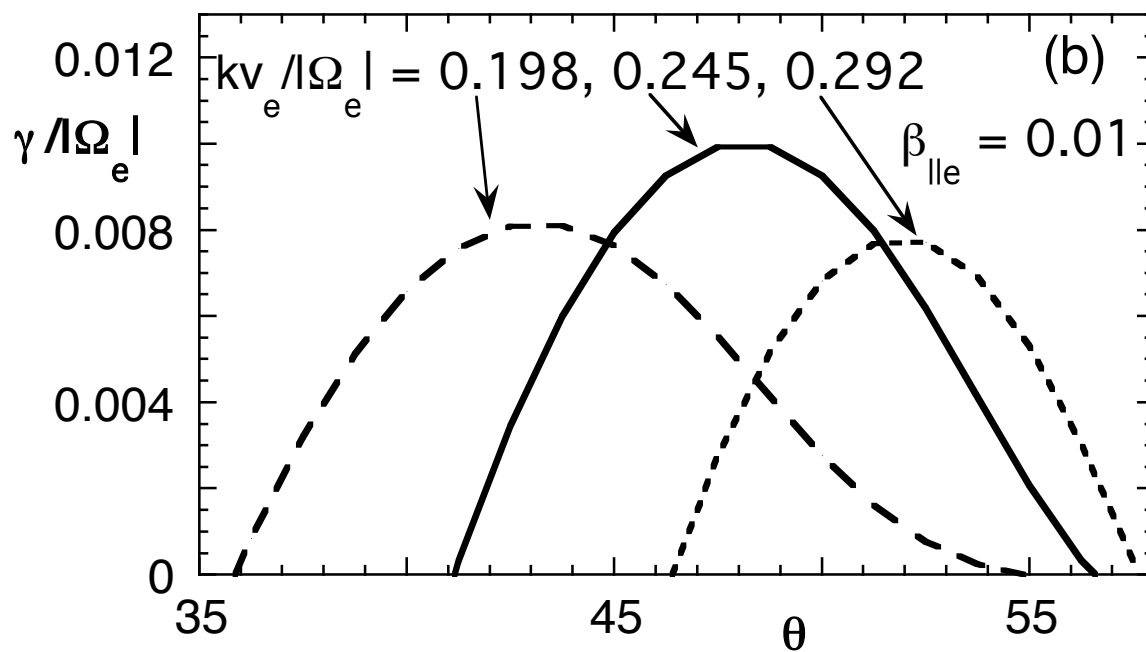
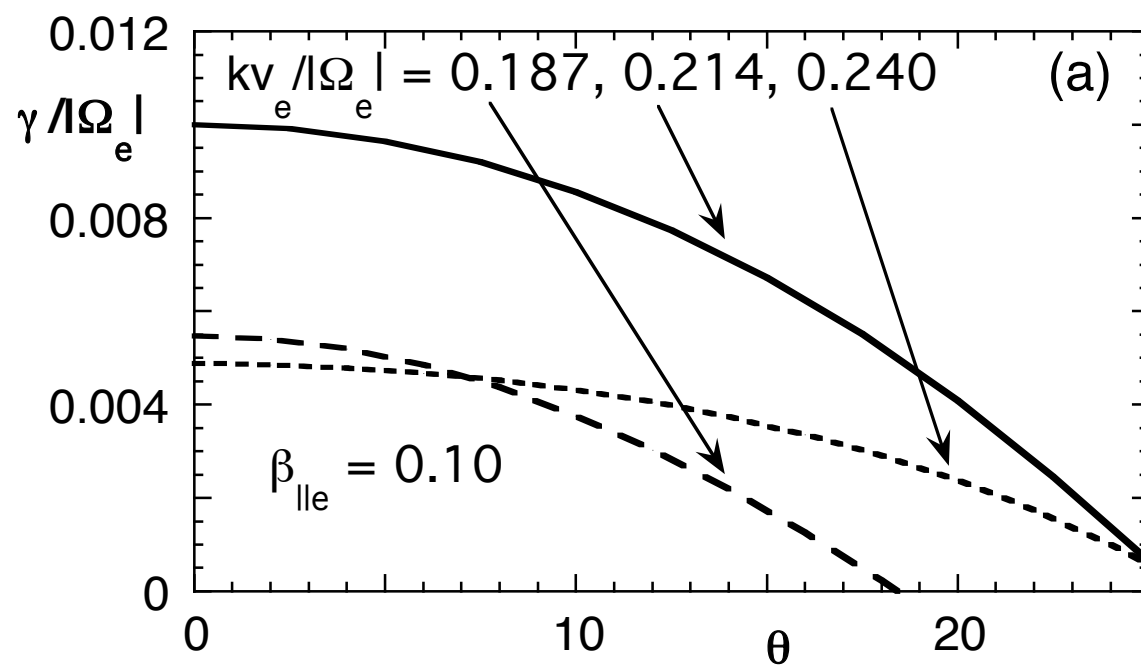


Figure 1

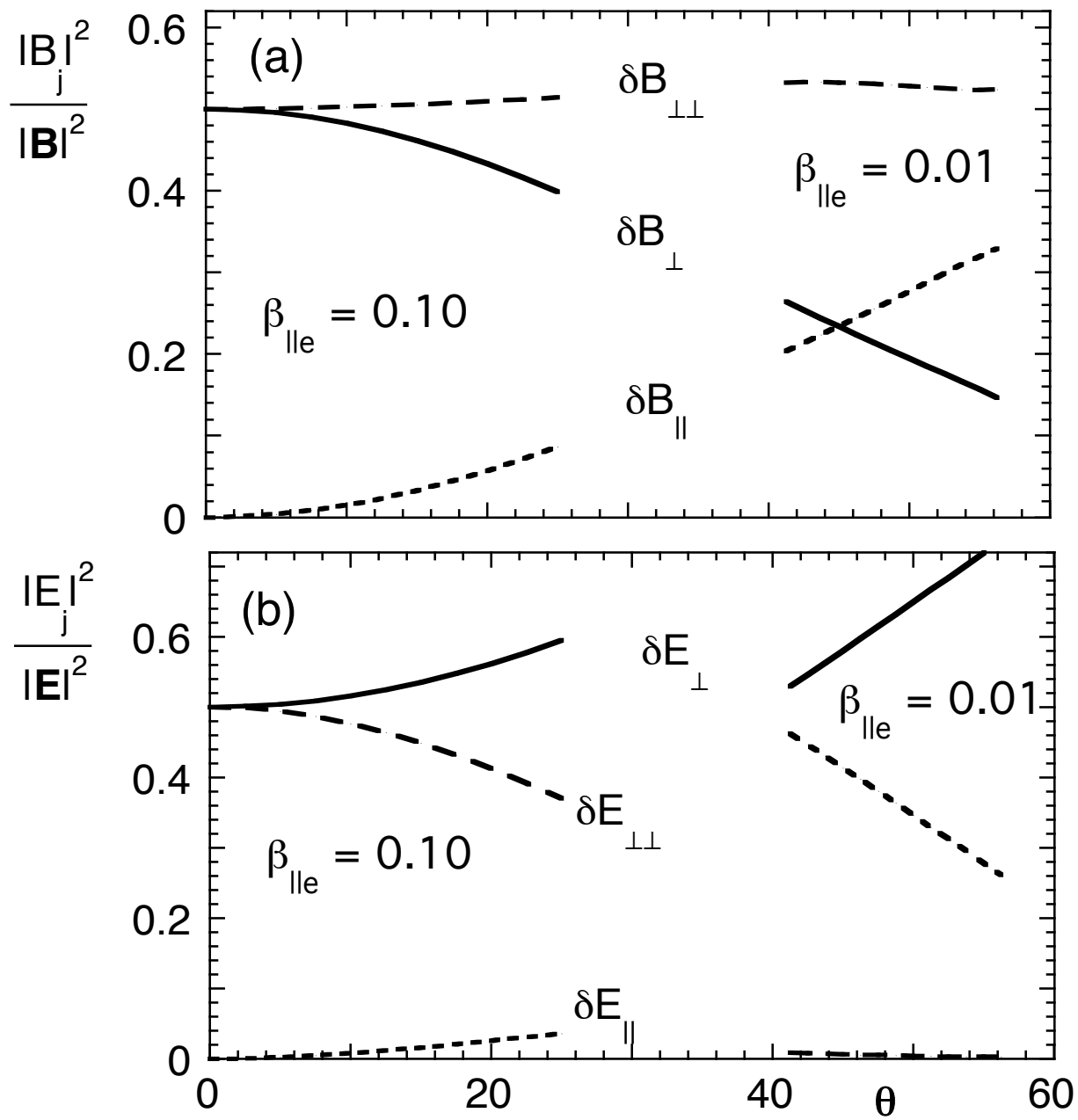
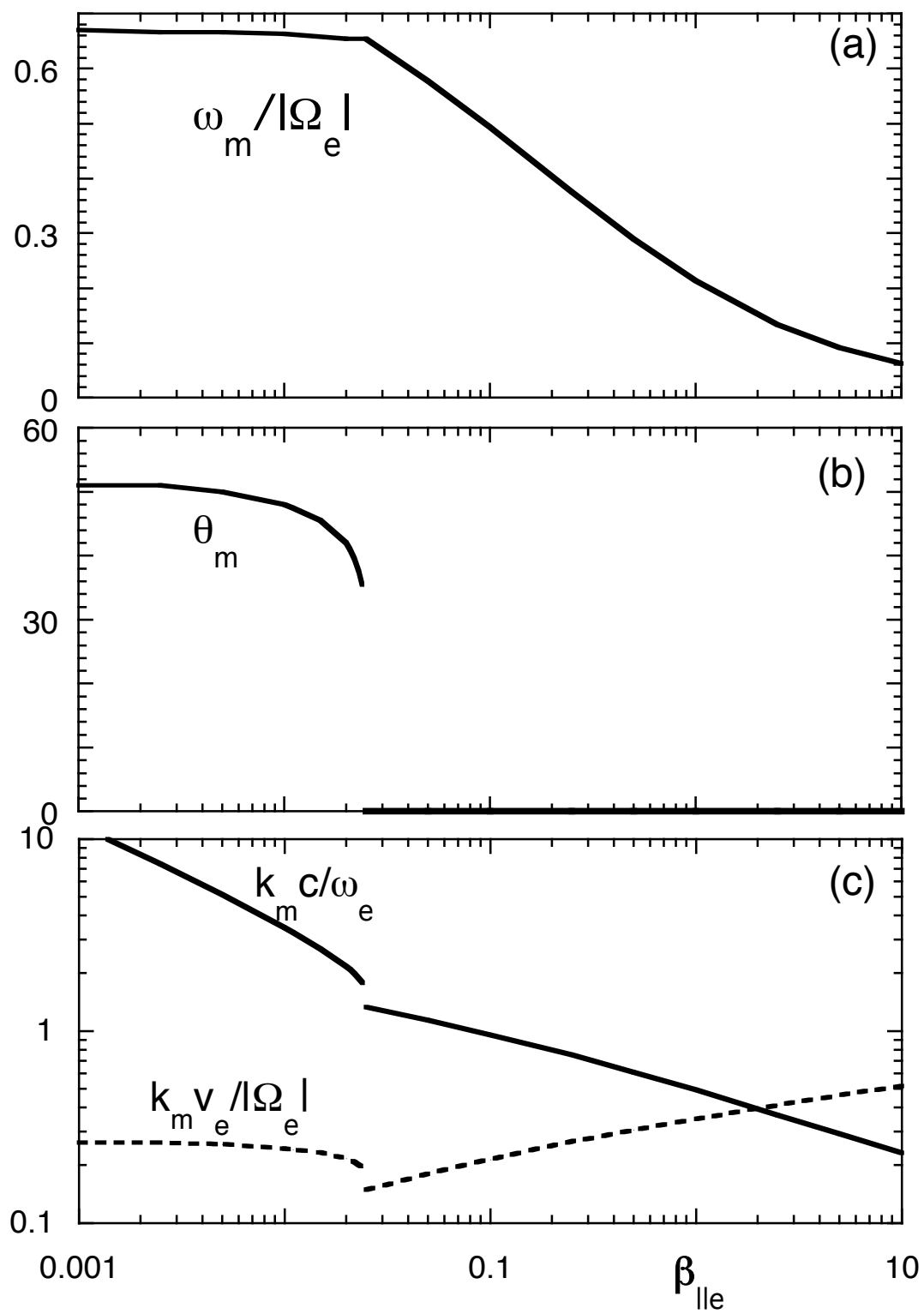


Figure 2



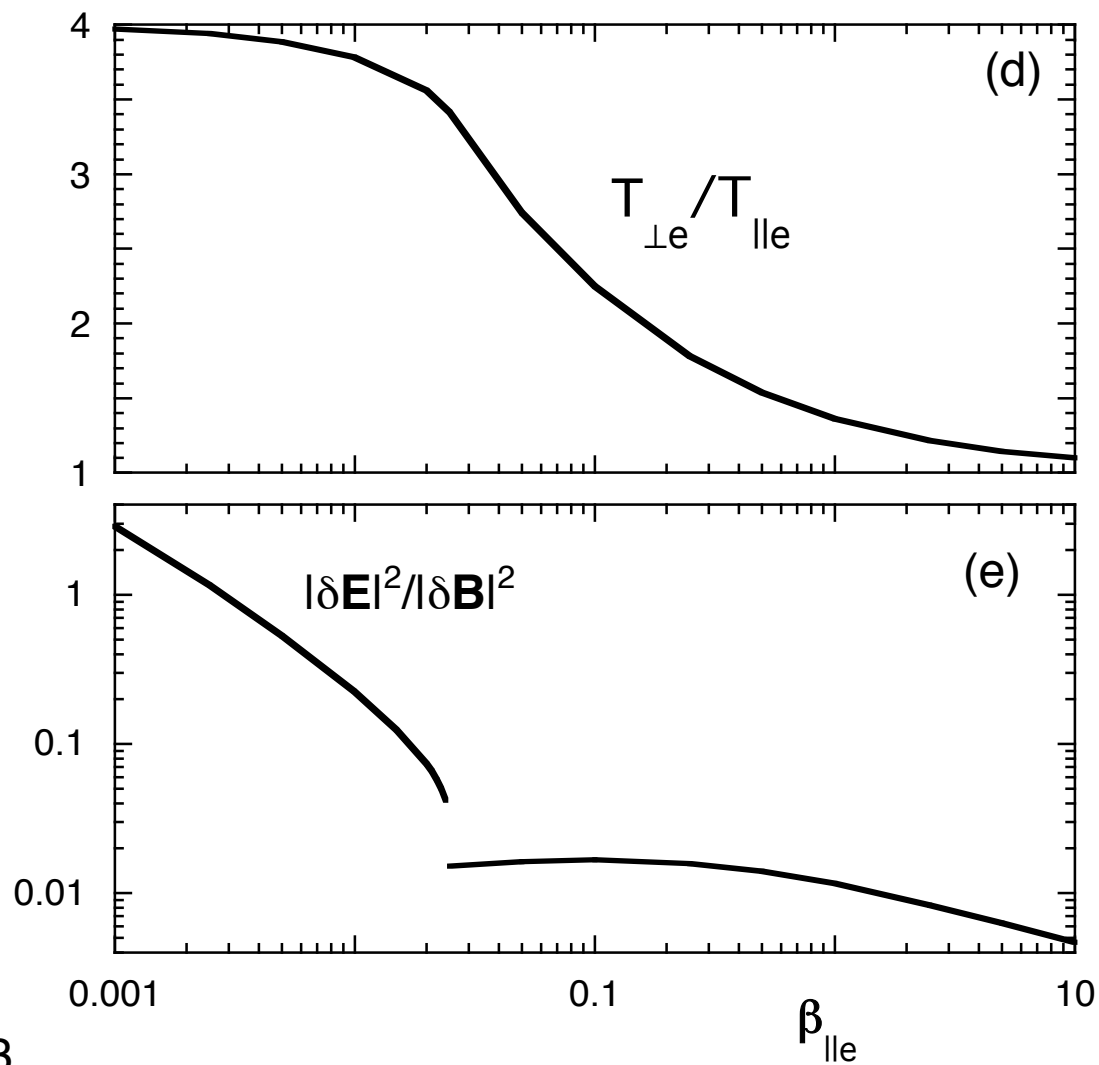


Figure 3

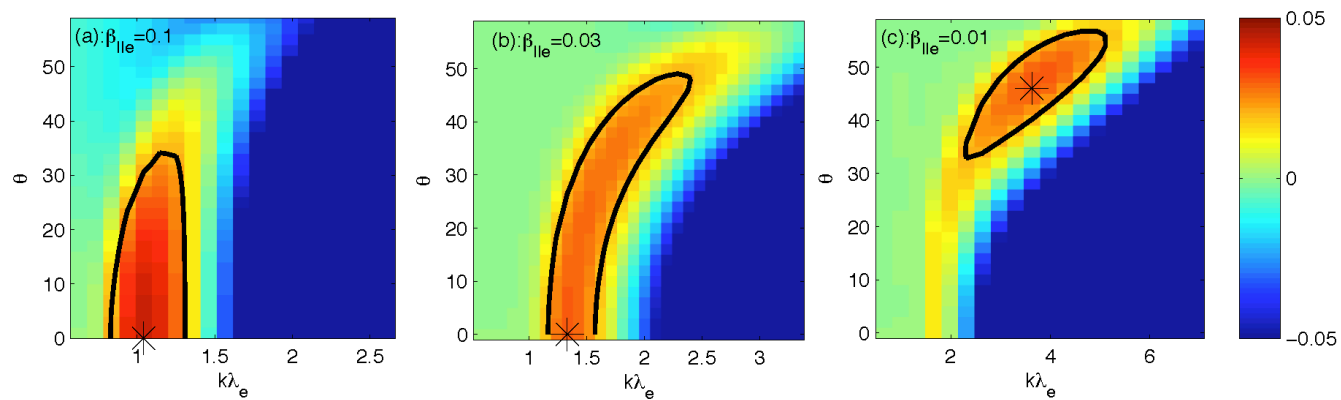


Figure 4

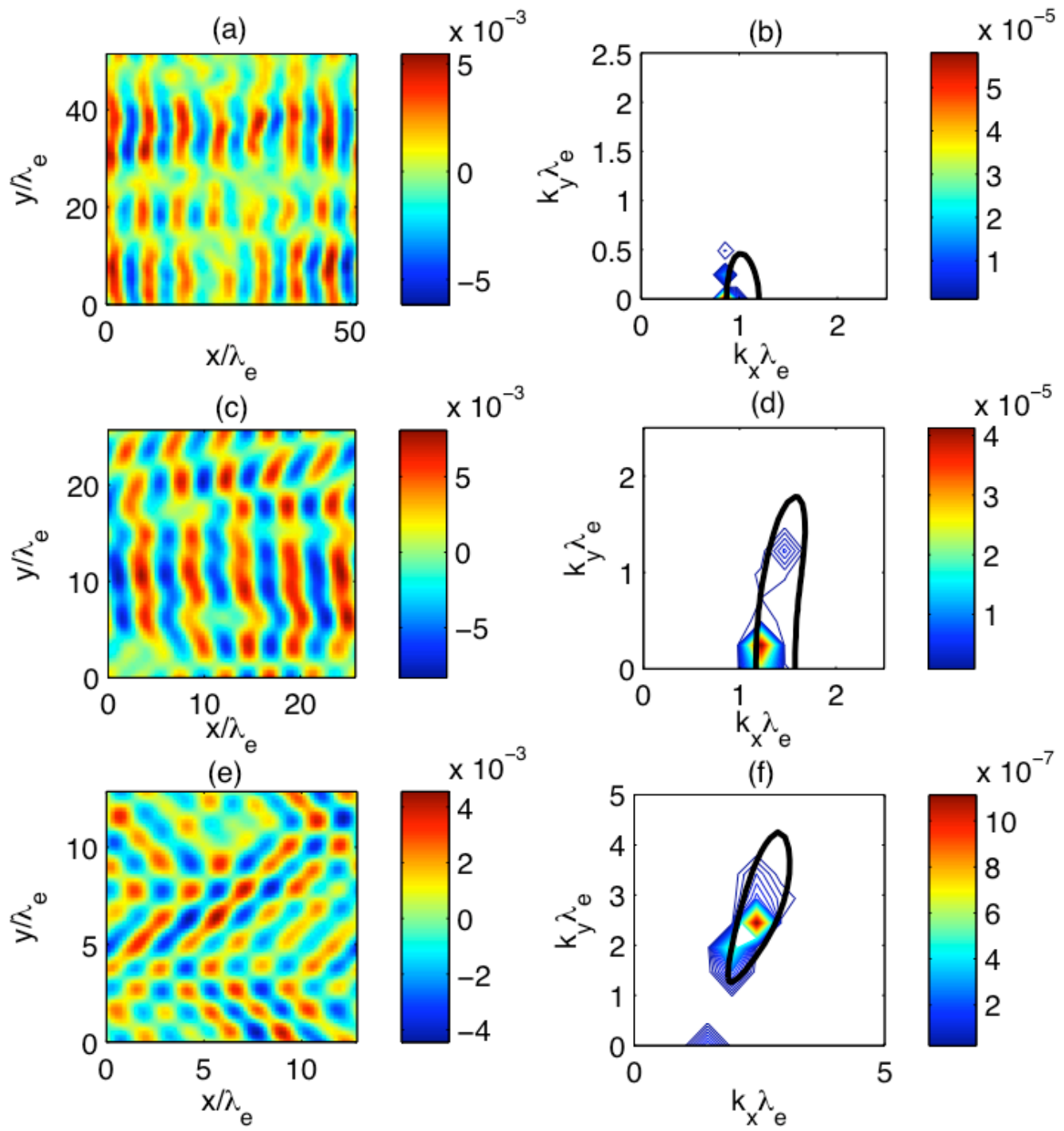


Figure 5



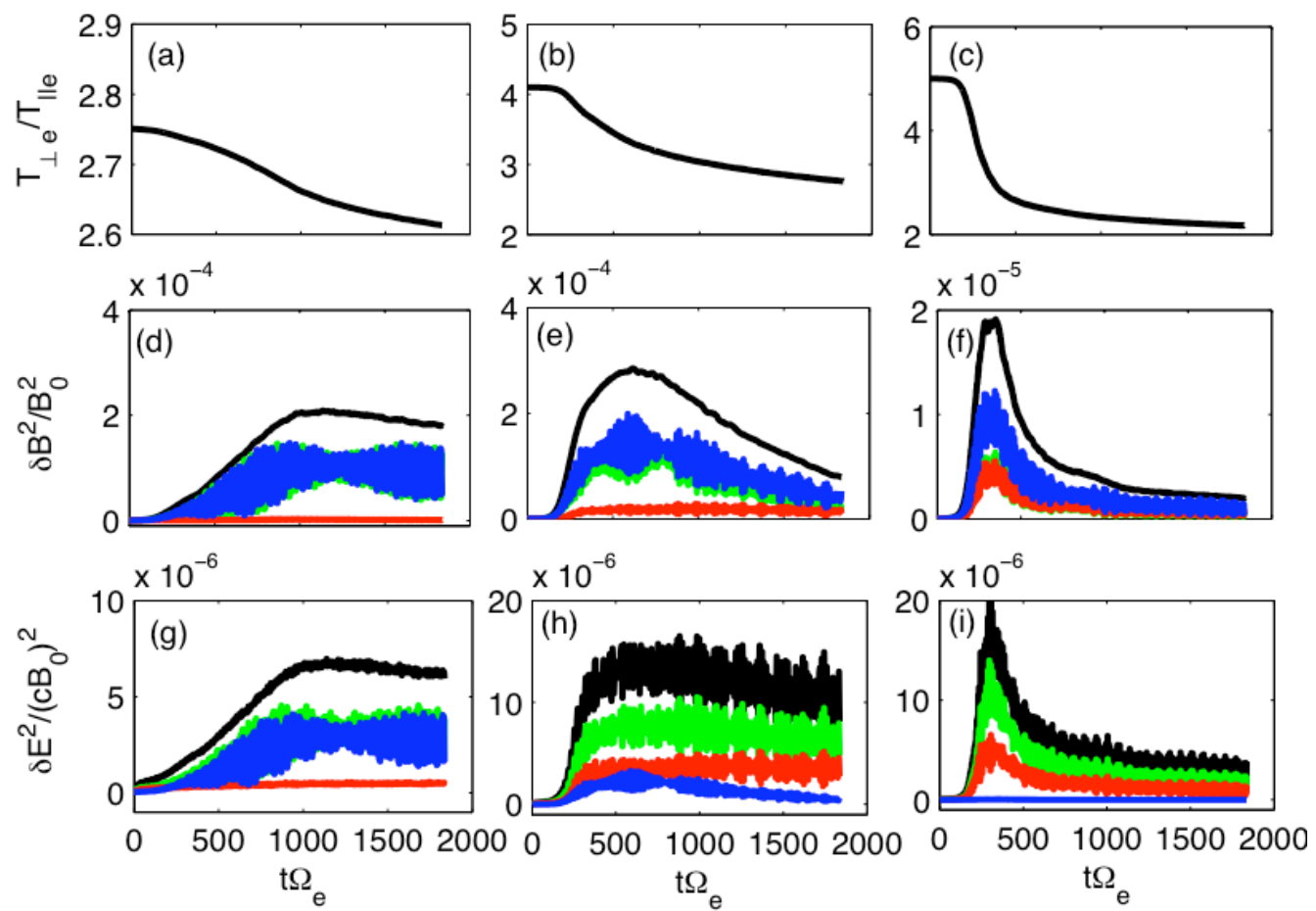


Figure 6

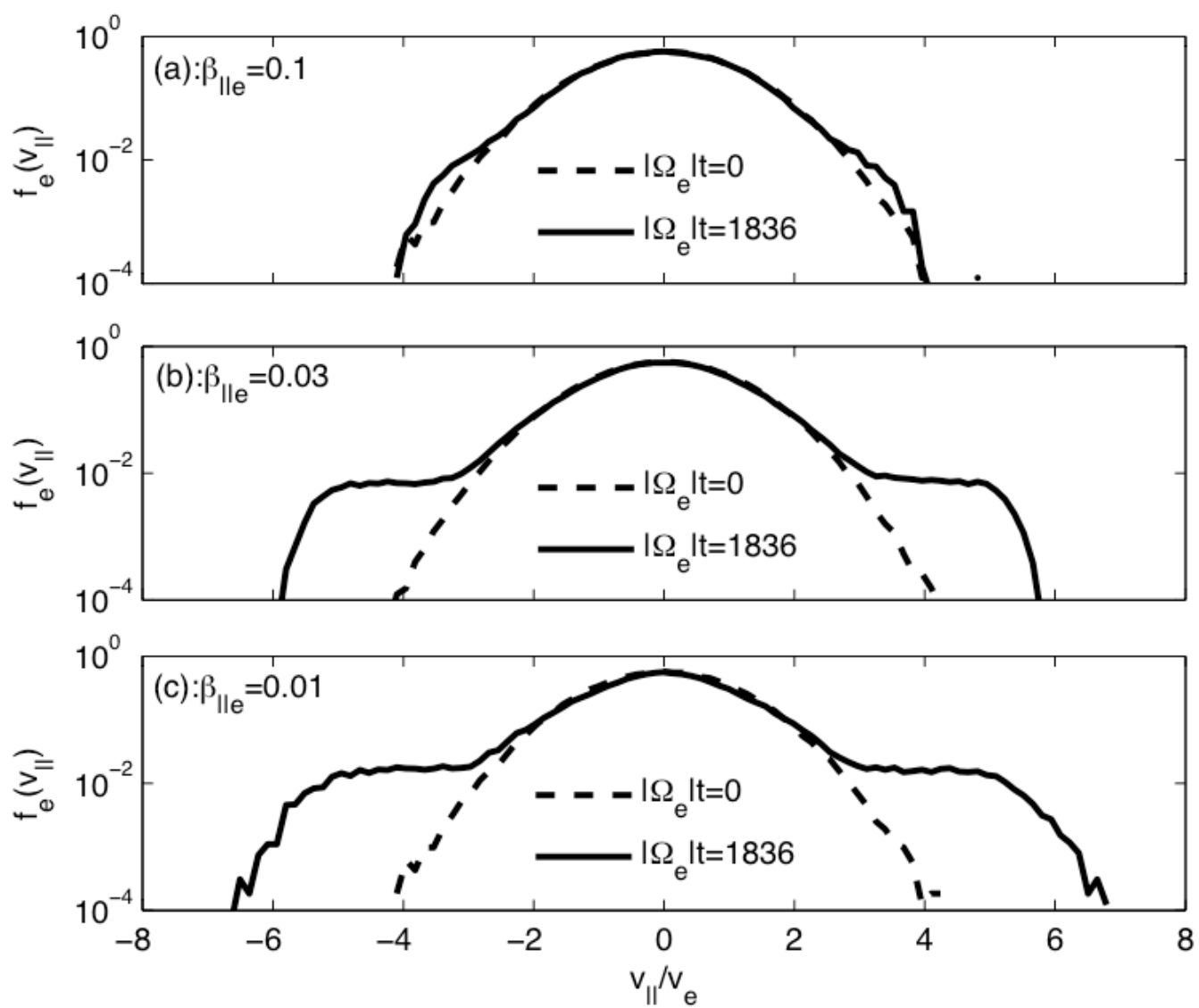


Figure 7

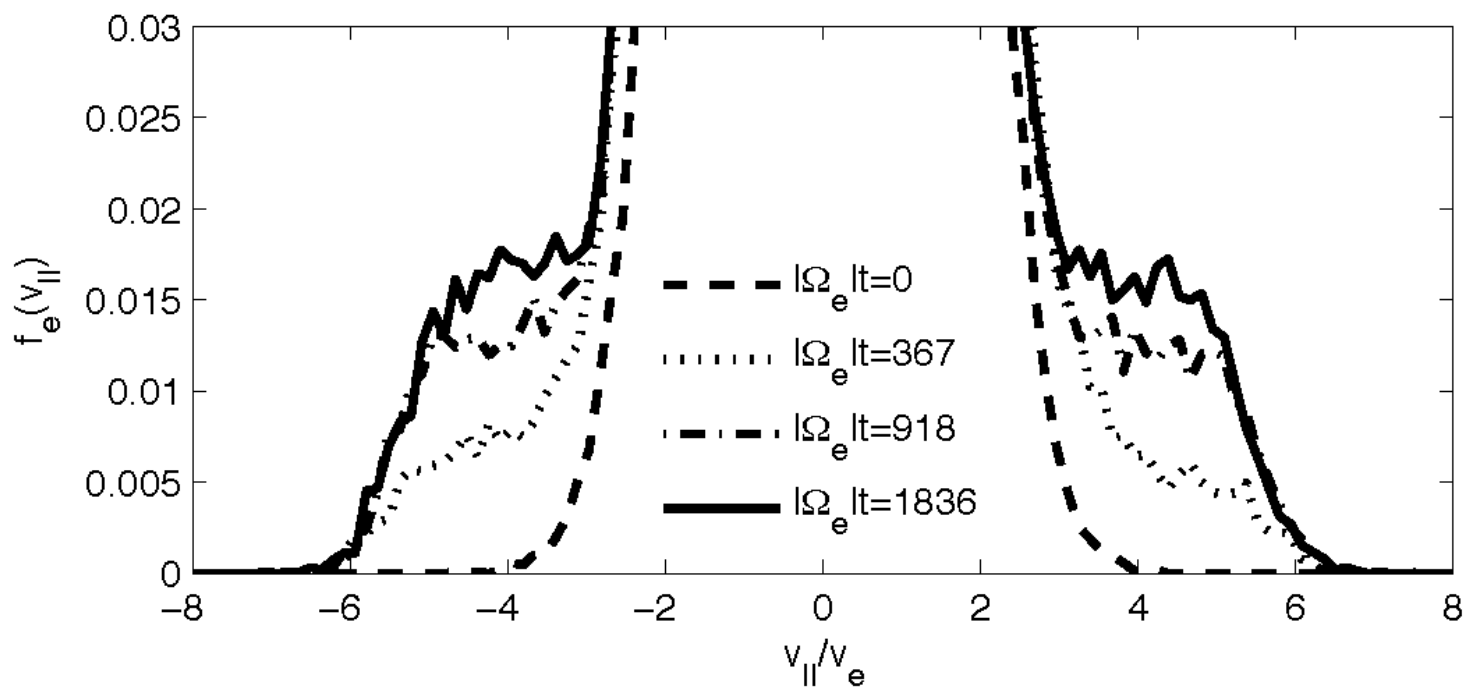


Figure 8